Monthly Notices
of the
ROYAL ASTRONOMICAL SOCIETY

MNRAS **496,** 598–611 (2020)
Advance Access publication 2020 April 3

doi:10.1093/mnras/staa1534

Linking the small-scale relativistic winds and the large-scale molecular outflows in the $z = 1.51$ lensed quasar HS 0810+2554

G. Chartas,[1★] E. Davidson,[1★] M. Brusa,[2,3★] C. Vignali,[2,3★] M. Cappi,[3] M. Dadina,[3] G. Cresci,[4] R. Paladino,[5] G. Lanzuisi[3] and A. Comastri[3]

[1]*Department of Physics and Astronomy, College of Charleston, Charleston, SC 29424, USA*
[2]*Dipartimento di Fisica e Astronomia dell'Università degli Studi di Bologna, via P. Gobetti 93/2, I-40129 Bologna, Italy*
[3]*INAF, Osservatorio di Astrofisica e Scienza dello Spazio di Bologna, via P. Gobetti 93/3, I-40129 Bologna, Italy*
[4]*INAF, Osservatorio Astrofisico di Arcetri, Largo Enrico Fermi 5, I-50125 Firenze, Italy*
[5]*INAF, Istituto di Radioastronomia, via Piero Gobetti 101, I-40129 Bologna, Italy*

Accepted 2020 May 27. Received 2020 May 27; in original form 2020 April 6

ABSTRACT

We present Atacama Large Millimeter/submillimeter Array (ALMA) observations of the quadruply lensed $z = 1.51$ quasar HS 0810+2554 which provide useful insight on the kinematics and morphology of the CO molecular gas and the ~ 2 mm-continuum emission in the quasar host galaxy. Lens modelling of the mm-continuum and the spectrally integrated CO(J = 3→2) images indicates that the source of the mm-continuum has an eccentricity of $e \sim 0.9$ with a size of ∼1.6 kpc and the source of line emission has an eccentricity of $e \sim 0.7$ with a size of ∼1 kpc. The spatially integrated emission of the CO(J = 2→1) and CO(J = 3→2) lines shows a triple peak structure with the outer peaks separated by $\Delta v_{21} = 220 \pm 19$ km s^{-1} and $\Delta v_{32} = 245 \pm 28$ km s^{-1}, respectively, suggesting the presence of rotating molecular CO line emitting gas. Lensing inversion of the high spatial resolution images confirms the presence of rotation of the line emitting gas. Assuming a conversion factor of $\alpha_{\rm CO} = 0.8$ M$_\odot$ (K km s^{-1} pc^2)$^{-1}$ we find the molecular gas mass of HS 0810+2554 to be $M_{\rm Mol} = (5.2 \pm 1.5)/\mu_{32} \times 10^{10}$ M$_\odot$, where μ_{32} is the magnification of the CO(J = 3→2) emission. We report the possible detection, at the 3.0–4.7σ confidence level, of shifted CO(J = 3→2) emission lines of high-velocity clumps of CO emission with velocities up to 1702 km s^{-1}. We find that the momentum boost of the large-scale molecular wind is below the value predicted for an energy-conserving outflow given the momentum flux observed in the small-scale ultrafast outflow.

Key words: gravitational lensing: strong – ISM: jets and outflows – galaxies: active – galaxies: high-redshift – quasars: general – quasars: individual: HS 0810+2554.

1 INTRODUCTION

Powerful small-scale X-ray absorbing winds have now been detected near the central supermassive black holes in several distant galaxies. These winds are believed to evolve into large-scale outflows that regulate the evolution of the host galaxies. The mechanism by which these small-scale winds transition into such important feedback mechanisms is not yet fully understood. Understanding the link between the small-scale relativistic winds of active galactic nuclei (AGNs) and the associated large-scale powerful molecular outflows in their host galaxies will thus provide valuable insight into the feedback process that regulates the growth of the supermassive black hole, the possible quenching of star formation and overall galaxy evolution. Theoretical models (e.g. Faucher-Giguère & Quataert 2012; Zubovas & King 2012) predict that AGN small-scale winds initially collide with the interstellar medium gas and transfer their momentum to the host galaxy gas (momentum-conserving phase). These models predict that at latter times the gas expands adiabatically in an energy-conserving mode with terminal velocities of about a few 1000 km s^{-1}. Testing these models requires the comparison of the kinematics and the energetics of the small and large-scale outflows in the same objects and in AGNs near the peak of AGN cosmic activity (i.e. at $z \sim 2-3$).

Observations of ultraluminous infrared galaxies (ULIRGs, e.g. Feruglio et al. 2010; Fischer et al. 2010; Sturm et al. 2011; Veilleux et al. 2013; Cicone et al. 2014; Brusa et al. 2018; Bischetti et al.

★ E-mail: chartasg@cofc.edu (GC); davidsonem@g.cofc.edu (ED); marcella.brusa@inaf.it (MB); cristian.vignali@unibo.it (CV)

2019; Sirressi et al. 2019; Smith et al. 2019) have revealed large-scale molecular outflows traced in OH and CO extending over kpc scales with velocities exceeding ∼1000 km s^{-1} and with massive outflow rates (up to ∼1200 M$_\odot$ yr^{-1}).

The presence of both small- and large-scale energy-conserving outflows were recently discovered by Tombesi et al. (2015), in the $z = 0.189$ ULIRG IRAS F11119+3257 (see also Veilleux et al. 2017, with updated estimates of the energy and momentum transfer in this object), and by Feruglio et al. (2015), in the $z = 0.04217$ ULIRG Mrk 231 (see also Longinotti et al. 2018; Bischetti et al. 2019; Mizumoto, Izumi & Kohno 2019). At $z > 1$, the only object where both small and large-scale outflows have been detected is the $z = 3.912$ BAL quasar APM 08279+5255, showing molecular gas outflowing with maximum velocity of $v = 1340$ km s^{-1} (Feruglio et al. 2017).

Another promising quasar to test feedback models is the $z = 1.51$ quadruply gravitationally lensed ULIRG HS 0810+2554 with a bolometric FIR luminosity (40–120 μm) of $L_{\rm FIR} = 10^{13.5}/\mu_{\rm FIR}\ L_\odot$, where $\mu_{\rm FIR}$ is the magnification factor in the FIR band (Stacey et al. 2018). The total bolometric luminosity of HS 0810+2554 is $L_{\rm Bol} = 10^{13.97}/\mu_{\rm UV}\ L_\odot$, based on the monochromatic luminosities at 1450 Å (Runnoe, Brotherton & Shang 2012), where $\mu_{\rm UV}$ ∼103 is the magnification factor in the UV band.

Our *Chandra* and *XMM–Newton* observations of HS 0810+2554 (Chartas et al. 2016) indicate (at >99 per cent confidence) the presence of a highly ionized and relativistic outflow in this highly magnified object. The hydrogen column density of the X-ray outflowing absorber lies within the range $N_{\rm Habs} = 2.9$–3.4×10^{23} cm^{-2}, and the outflow velocity components lie within the range $v_{\rm out} = 0.1$−$0.4c$. The mass-outflow rate of the X-ray absorbing material of HS 0810+2554 is found to lie in the range of $\dot{M} = 1.5$−3.4 M$_\odot$ yr^{-1} and is comparable to the accretion rate of ∼1 M$_\odot$ yr^{-1}. UV spectroscopic observations with VLT/UVES (Chartas et al. 2016) indicate that the UV absorbing material of HS 0810+2554 is outflowing at $v_{\rm UV}$ ∼19 400 km s^{-1}. VLA observations of HS 0810+2554 (Jackson et al. 2015) at 8.4 GHz have revealed radio emission in this radio-quiet object.

More recently, Hartley et al. (2019) using e-MERLIN and European VLBI Network observations have identified jet activity in HS 0810+2554. Specifically, their source reconstruction of the radio and *HST* data of HS 0810+2554 shows two jet components linearly aligned on opposing sides of the optical quasar core. Stacey et al. (2018) found that HS 0810+2554 falls on the radio−FIR correlation, even though, the observations of Hartley et al. show that the radio emission of HS 0810+2554 arises predominately from a jetted quasar. Consequently they suggest that the radio−FIR correlation cannot always be used to rule out AGN activity in favour of star formation activity. We also note that the SED template fit to HS 0810+2554 indicates that the AGN contribution in this object is significant (Rowan-Robinson & Wang 2010) and a strong starburst in this object is unlikely. Specifically, the ratio of the torus to optical luminosity of HS 0810+2554 is found to be $L_{\rm torus}/L_{\rm opt}$ ∼0.5, which can be interpreted as a dust covering factor.

We expect that the small-scale ultrafast outflows (UFOs) in HS 0810+2554 may be driving a larger scale outflow of molecular gas in the host galaxy. To investigate the possible presence of a large-scale outflow, we obtained ALMA observations of HS 0810+2554 in cycle 5. The main goals of our ALMA observations were to (a) spatially resolve the continuum mm emission emitted in the host galaxy of HS 0810+2554 and infer its physical extent, and (b) detect the molecular gas in CO(J = 3→2) and CO(J = 2→1), measure the total molecular CO mass and its extent, and search for a possible outflow.

In Section 2, we present the ALMA observations and data reduction of HS 0810+2554. In Section 3, we present the analysis of the mm-continuum emission. In Section 4, we present the analysis of the CO(J = 3→2) emission performed with the ALMA extended configuration. In Section 5, we present the analysis of the CO(J = 3→2) and CO(J = 2→1) emission performed with the ALMA compact configuration. In Section 6, we present the results of our lensing analysis to explain the offset between the optical and mm image positions and our results from modelling the spatially integrated spectra of the CO(J = 3→2) and CO(J = 2→1) emission lines. In Section 7, we present the possible detection of outflows of CO(J = 3→2) emitting molecular gas. Finally, in Section 8 we present a discussion of our results and conclusions. Throughout this paper we adopt a flat Λ cosmology with $H_0 = 68$ km s^{-1} Mpc^{-1} $\Omega_\Lambda = 0.69$, and $\Omega_{\rm M} = 0.31$ (Planck Collaboration XIII 2016).

2 ALMA OBSERVATIONS AND DATA REDUCTION

HS 0810+2554 was observed with ALMA during cycle 5 (project 2017.1.01368) in Band 3 (100 GHz) and Band 4 (140 GHz), where the redshifted CO(J = 2→1) and CO(J = 3→2) transitions are

Table 1. Log of ALMA observations of HS 0810+2554.

Date[a]	$t_{\rm int}$ [b] (s)	Beam [c]	SPW[d]	Width[e] (GHz)	Channels[f]	Resolution[g] (km s^{-1})	Effective resolution[h] (km s^{-1})	Band
2017 Nov 30	1655	0.12 arcsec × 0.06 arcsec	138.0/139.9/150.0/152.0	2	128	34.0	34.0	4
2018 Jan 28	1716	1.10 arcsec × 0.81 arcsec	91.8/ 90.2/102.3/104.2	1.875	1920	3.2	25.6	3
2018 Aug 29	544	1.48 arcsec × 1.03 arcsec	137.8/135.9/149.8/147.9	1.875	1920	2.1	8.4	4

[a]Date of start of observation.
[b]Total integration time on source.
[c]The beam size obtained by adopting the Briggs weighting scheme and a robust parameter of $R = 2$.
[d]The central frequencies of the spectral windows.
[e]The width of each spectral window.
[f]The number of channels in each spectral window.
[g]The velocity resolution at the frequency of the CO line present in the spectral window.
[h]The effective velocity resolution obtained after binning the spectra.

visible, respectively. Table 1 summarizes the observation dates, source integration science times, and spectral configuration.

The Band 3 observations have been taken in one session in the configuration C43-5, with a maximum baseline of 1.4 km, providing a spatial resolution of ∼1 arcsec. The spectral configuration used provided 1920 channels with a spectral resolution of 3.2 km s^{-1}. The Band 4 observations have been taken in two sessions: the first one with the extended configuration C43-7, providing a spatial resolution of ∼0.1 arcsec, in TDM (Time Division Mode) spectral configuration, with 128 channels, 34 km s^{-1} wide. The second session has been taken with a more compact configuration, C43-3, providing a resolution of ∼1.2 arcsec, and a higher spectral resolution, 1920 channels, 2.1 km s^{-1} wide.

Each ALMA data set has been calibrated using the ALMA pipeline (version Pipeline-CASA51-P2-B). The calibrated data have been imaged and analysed with the CASA software (version 5.1.1-5). The images of continuum emission in both bands have been obtained running the CASA task *tclean* in the multifrequency synthesis (mfs) mode on the visually selected line-free channels of the observed spectral ranges. To obtain the maximum sensitivity we used the Briggs weighting scheme with the robust parameter set to 2 (natural weighting). The achieved rms in the continuum images are 16 μJy beam^{-1} in Band 3 and 13 and 29 μJy beam^{-1} in the Band 4 high and low spatial resolution images, respectively.

Prior to creating the CO line cubes, the continuum has been subtracted from the data sets using the CASA task *uvcontsub*. A linear fit of the continuum in the visually selected line-free channels of the spectral windows has been calculated in the visibility plane and subtracted from the full spectral range. The datacube for the high spatial resolution image in Band 4 has been obtained using the original spectral resolution of the data (34 km s^{-1}). The datacubes for the Band 3 and Band 4 low spatial resolution images have been obtained by binning the spectra by factors of 8 and 4, respectively (reaching velocity resolutions of 25.6 and 8.4 km s^{-1}, respectively).

The natural weighting scheme, which was used for the continuum images, has also been applied to the CO line cubes to enhance the sensitivity. The rms values achieved in the line datacubes have been measured in line-free channels and are found to be ∼150 μJy beam^{-1} for a 34.0 km s^{-1} channel width in Band 4 (extended configuration), ∼390 μJy beam^{-1} for a 25.6 km s^{-1} channel width in Band 3 (compact configuration), and ∼750 μJy beam^{-1} for a 34.0 km s^{-1} channel width in Band 4 (compact configuration). We finally obtained the integrated intensity images (moment 0 maps) of each datacube, using the task *immoments*.

3 ANALYSIS OF THE MM-CONTINUUM EMISSION OF HS 0810+2554.

A mm-continuum image was created from the high spatial resolution data set using mfs with the channels containing the CO(J = 3→2) line removed. In Fig. 1, we show the *HST* ACS *F555W* image of HS 0810+2554 with the ALMA band 4 continuum contours overlaid. The *HST* and the ALMA band 4 continuum images were aligned relative to the isolated image D. The mm-continuum lensed images of the sources A and B are detected as extended emission at a combined significance level of ∼10σ, however, images C (∼1.6σ) and D (∼2.3σ) barely rise above the noise level (see Table 2).

In Table 2, we list the relative positions of the *HST* image positions with respect to image A taken from the CfA-Arizona Space Telescope LEns Survey (CASTLES) of gravitational lenses,

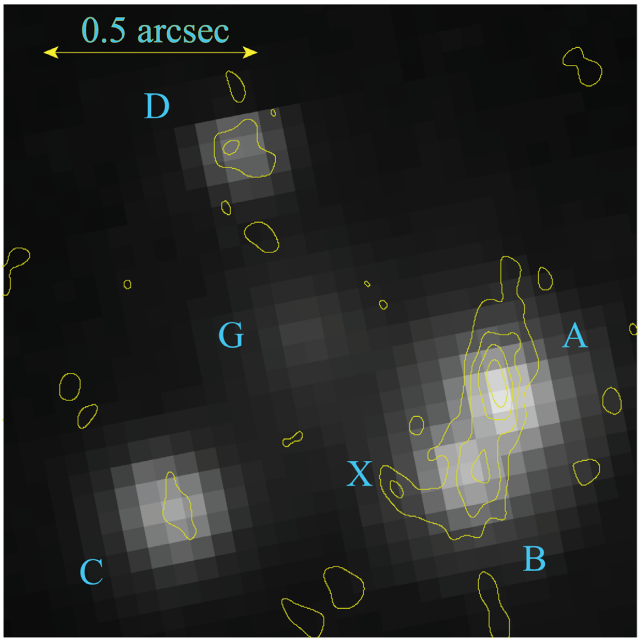

Figure 1. The *HST* ACS *F555W* image of the lensed $z = 1.51$ quasar HS 0810+2554 with the *ALMA* band 4 continuum contours overlaid. The offset between the optical and the mm-continuum images can be explained by lensing effects and different emission locations and sizes of the optical and mm-emission regions. The mm-continuum image shows a new feature labelled X near image B that is not present in the optical. G is the lens galaxy. The contours represent the ∼2 mm-continuum [−3, −2, 2, 3, 4, 5]σ levels, where 1σ = 12.7 μJy beam^{-1}.

the relative positions of the ALMA continuum images with respect to A and the mm-continuum flux densities of the images. The peaks of the mm-continuum images A and B are found to be offset at the >10σ level from the optical centroids when aligning the optical and mm-continuum maps to the isolated image D. This offset is investigated in the lens modelling of HS 0810+2554 presented in Section 6.

The mm-continuum emission also shows a new feature labelled X near image B that is not present in the optical image. Component X also does not align with any of the radio components resolved in the e-MERLIN observations at 4.32 and 5.12 GHz of HS 0810+2554 (Hartley et al. 2019).

The flux density of the continuum of the combined images at a mean frequency of 143 GHz is estimated to be (401 ± 50 μJy)/$\mu_{\rm cont}$, where $\mu_{\rm cont} = 7 \pm 3$ is the lensing magnification of the mm-continuum emitting region estimated in Section 6.

The mm-continuum flux density of HS 0810+2554 was also estimated from the low spatial resolution observations. Specifically, for the 2018 August and March observations performed in Band 4, the mm-continuum image was created using mfs with the channels containing the CO(J = 3→2) line removed. For the 2018 January observation performed in Band 3, the channels containing the CO(J = 2→1) line were removed. To estimate the flux density of the continuum we used the CASA tool 2D Fit with the fitting region set to a circle of radius of 2.5 arcsec centred on the source. We find the flux densities of the continuum at mean frequencies of 143 and 97 GHz to be (400 ± 38 μJy)/$\mu_{\rm cont}$ and (197 ± 49 μJy)/$\mu_{\rm cont}$, respectively. As we predicted, the observed ALMA flux densities are found to be just below the 3σ upper limit of ∼1 mJy inferred

Table 2. ALMA positions and integrated flux densities of the lensed images (A, B, C, and D) of the mm-continuum of HS 0810+2554. For comparison, we also list the relative *HST* positions of the lensed optical images.

Image	RA	Dec.	RA	Dec.	$S_{2.2\ mm}$[c]
	ALMA mm-continuum[a]		*HST* (CASTLES)[b]		
	(arcsec)	(arcsec)	(arcsec)	(arcsec)	(μJy)
A	0	0	0	0	168 ± 31
B	+0.050 ± 0.005	−0.192 ± 0.005	+0.087 ± 0.003	−0.163 ± 0.003	131 ± 31
C	+0.767 ± 0.005	−0.302 ± 0.005	+0.774 ± 0.003	−0.257 ± 0.003	27 ± 18
D	+0.643 ± 0.005	+0.577 ± 0.005	+0.610 ± 0.003	+0.579 ± 0.003	41 ± 18
X	+0.247 ± 0.005	+0.247 ± 0.005			34 ± 18

[a]The ALMA mm-continuum images A and B are extended. The ALMA RA and Dec. positions correspond to the centroids the extended images.
[b]The *HST* image positions are taken from the CASTLES of gravitational lenses website http://cfa-www.harvard.edu/glensdata/.
[c]Flux densities of the ALMA images with the continuum integrated between 1.97 and 2.17 mm. The fractional flux errors based on calibration are $\sigma_F / F \sim 5$ per cent

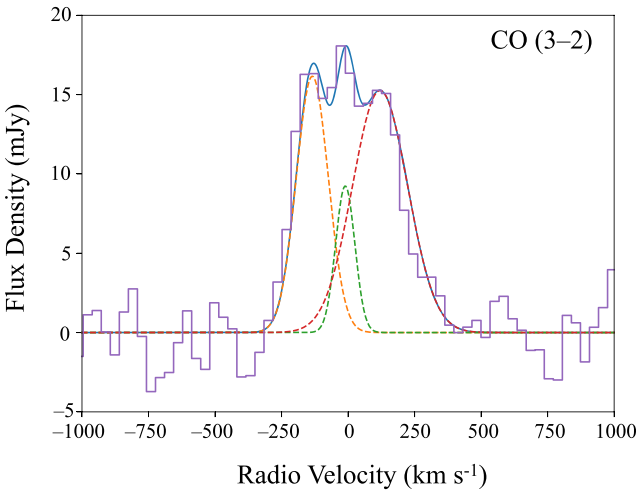

Figure 2. The ALMA CO(J = 3→2) continuum-subtracted spectrum of HS 0810+2554 obtained with the ALMA extended configuration. The spectral line is fit with a model that consists of three Gaussians. The velocity shifts can be explained with the presence of a rotating molecular disc. We have assumed a systemic redshift of $z = 1.50849 \pm 0.00002$ based on the redshift of the [O III] line detected in the SINFONI spectrum of HS 0810+2554 (Cresci et al., in preparation).

from the non-detection of HS 0810+2554 by CARMA (Riechers 2011).

4 THE EINSTEIN RING OF THE CO(J = 3→2) EMISSION IS RESOLVED WITH THE ALMA EXTENDED CONFIGURATION

The image of the CO(J = 3→2) line emission was produced from the continuum-subtracted data, in the frequency range 137.714–137.980 GHz. Also in this case, we used natural weighting to maximize the S/N (Briggs parameter $R = 2$) for our image of the line emission. A spatially integrated spectrum was extracted from a circular region centred on HS 0810+2554 with a radius of 0.7 arcsec. The resulting spectrum shown in Fig. 2 shows a prominent (S/N ∼9) emission line with a clear asymmetric triple peaked structure. The spectrum was initially fit with a model consisting of a single Gaussian. This fit is not acceptable in a statistical sense with $\chi^2/\nu = 189/16$, where ν are the degrees of freedom. We next use a model consisting of three Gaussians. The fit with three Gaussians results in an acceptable fit with $\chi^2/\nu = 11.4/10$. The best-fitting parameters of the centroid velocities and full width at half-maxima (FWHM) were found to be (v_1, FWHM$_1$) = (−134 ± 10, 142 ± 22 km s^{-1}), (v_2, FWHM$_2$) = (−11 ± 11, 85 ± 31 km s^{-1}), and (v_3, FWHM$_3$) = (120 ± 21, 244 ± 39 km s^{-1}). The dominant blue and red peaks of the CO(J = 3→2) line profile are suggestive of rotation. If this is the case, then the velocity separation between the outer peaks corresponds to a rotational velocity of ∼250 km s^{-1} (without a correction for inclination). The CO line profiles of lensed AGNs will in general be distorted by differential magnification across the molecular disc (e.g. Rybak et al. 2015; Leung, Riechers & Pavesi 2017; Paraficz et al. 2018). In Section 7, as part of our lens modelling we derive the moment 1 velocity map of the CO(J = 3→2) line emission of HS 0810+2554 calculated in the source plane. This velocity map clearly shows disc rotation with a velocity range that is consistent with the CO(J = 3→2) line profile. We have assumed a systemic redshift of $z = 1.50849 \pm 0.00002$ based on the redshift of the [O III] line detected in the Spectrograph for INtegral Field Observations in the Near Infrared (SINFONI) spectrum of HS 0810+2554 (Cresci et al., in preparation). The integrated flux density of the CO(J = 3→2) emission line is (6.8 ± 0.8 Jy km s^{-1})/μ_{32}, where μ_{32} is the lensing magnification of the CO(J = 3→2) emitting region estimated in Section 6. The integrated flux densities of the three best-fitting Gaussian lines that make up the CO(J = 3→2) line (see Fig. 2) are $S_1 = 2.37 \pm 0.56$ Jy km s^{-1}, $S_2 = 0.84 \pm 0.16$ Jy km s^{-1}, and $S_3 = 3.55 \pm 0.40$ Jy km s^{-1}. The rms noise will mostly affect the estimated integrated flux density of the weakest central line component. However, as we show in Section 5, the central line component is also detected in the spectra of the CO(J = 3→2) and CO(J = 2→1) lines obtained with the ALMA compact configuration.

We produced spectrally integrated maps (moment 0 images) of the line and continuum emission components by integrating over the entire spectrum of these components. In Fig. 3, we show a raster image of the moment 0 map of the CO(J = 3→2) line with overlaid contours. The moment 0 map of the CO(J = 3→2) line shows that the line emission forms a partial Einstein ring in addition to emission centred around the 4 images A, B, C, and D. A clear offset

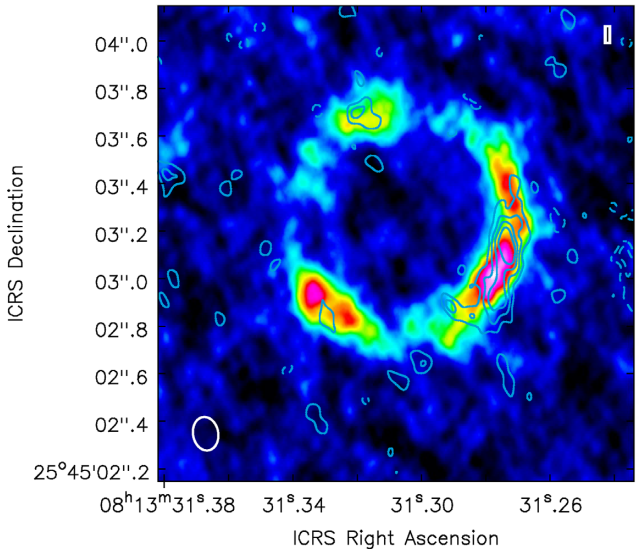

Figure 3. The ALMA CO(J = 3→2) moment 0 line emission of HS 0810+2554 with the 2 mm ALMA continuum overlaid as contours. The ALMA synthetic beam size is 0.1 arcsec × 0.06 arcsec and is indicated with the solid white ellipse in the lower left corner. The CO(J = 3→2) is clearly more extended along an Einstein ring than the 2 mm-continuum emission. The contours represent the ∼2 mm-continuum [−3, −2, 2, 3, 4, 5]σ levels, where 1σ = 12.7 μJy beam^{-1}. Solid and dashed contours represent positive and negative values.

is present between the peaks of images A and B in the lensed mm-continuum and CO(J = 3→2) line emission of HS 0810+2554 in the sense that the line connecting the mm-continuum peaks of images A and B is rotated counter-clockwise with respect to the tangent to the CO(J = 3→2) Einstein ring at the mid-point between these images. This offset is similar to the offset shown in Fig. 1 between the peaks of images A and B in the optical and mm-continuum emission.

Gravitational lensing of HS 0810+2554 stretches the extended CO(J = 3→2) source emission in each image along the Einstein radius. Spectra extracted along the Einstein radius show a Doppler shift of the centroid of the CO(J = 3→2) line as the spectral extraction region is moved along the Einstein radius. We illustrate the disc rotation in Fig. 4 by showing the CO(J = 3→2) spectra extracted from four different locations on the Einstein ring near the brightest isolated image C. The observed Doppler shift is consistent with a rotating CO(J = 3→2) emission region.

In Fig. 5, we show the position velocity diagrams for images A + B, C, and D of the high spatial resolution CO(J = 3→2) image cube of HS 0810+2554. Note that images A and C have positive parity and images B and D have negative parity (mirrored images of the source). The position velocity diagrams were created using the CASA task *impv* and are computed over three slices in the direction plane centred on images A + B, C, and D. The slices are shown in Fig. 4. A single slice is used to construct the position velocity diagram of images A + B since the elongated images A and B overlap. The widths of the slices are 0.25 arcsec. The offsets are with respect to the centre of the slices. The start and endpoint positions of the slices correspond to negative and positive offsets following the Einstein ring along the clockwise direction.

5 ANALYSIS OF THE CO(J = 3→2) AND CO(J = 2→1) EMISSION LINES OBTAINED WITH THE ALMA COMPACT CONFIGURATION

The images of the CO(J = 3→2) and CO(J = 2→1) line emission of HS 0810+2554 observed with the ALMA compact configuration were produced by subtracting the continuum spectral component from the spectral channels containing the CO(J = 3→2) line in the frequency range 137.7 GHz to 138.0 GHz and CO(J = 2→1) line in the frequency range 91.8 GHz to 92.0 GHz. In Fig. 6, we show the moment 0 images of the CO(J = 3→2) and CO(J = 2→1) line emissions overlaid with [−2, 2, 4, 6, 8]σ contours on the line emissions, where σ is the rms sensitivity.

We used natural weighting for our image of the line emission. Spatially integrated spectra of the CO(J = 3→2) and CO(J = 2→1) line emission were extracted from circular regions centred on HS 0810+2554 with radii of 3 arcsec. The resulting spectra shown in Fig. 7 show multiple peaks.

The CO(J = 3→2) spectrum was initially fit with a model consisting of a single Gaussian. This fit is not acceptable in a statistical sense with χ^2/ν = 49/23, where ν are the degrees of freedom. We next use a model consisting of three Gaussians. The fit with three Gaussians results in an acceptable fit with χ^2/ν = 18.5/17.The best-fitting parameters for the centroid velocities and FWHM of the CO(J = 3→2) line were found to be (v_1, FWHM$_1$) = (−124 ± 22, 151 ± 45 km s^{-1}), (v_2, FWHM$_2$) = (−28 ± 9, 51 ± 28 km s^{-1}), and (v_3, FWHM$_3$) = (104 ± 15, 221 ± 35 km s^{-1}). The integrated flux density of the CO(J = 3→2) emission line is (4.8 ± 1.3 Jy km s^{-1})/μ_{32}, where μ_{32} is the lensing magnification of the CO(J = 3→2) emitting region estimated in Section 6. We also independently estimated the flux density of the CO(J = 3→2) emission line using the `uvmodelfit` command that fits a single-component source model to the UV data. Using `uvmodelfit` with the argument `comptype` set for a Gaussian component model we find an average flux density of I = (8.4 ± 0.2 mJy)/$\mu_{\rm line}$ within a spectral window of width 544 km s^{-1}. The best-fitting parameters of the properties of the CO(J = 3→2) lines obtained with the extended and compact configurations are consistent within the error bars.

The CO(J = 2→1) spectrum was initially fit with a model consisting of a single Gaussian. This fit is not acceptable in a statistical sense with χ^2/ν = 39.5/15, where ν are the degrees of freedom. We next use a model consisting of three Gaussians. The fit with three Gaussians results in an acceptable fit with χ^2/ν = 11.1/9. The best-fitting parameters for the velocity centroids and FWHM of the CO(J = 2→1) line were found to be (v_1, FWHM$_1$) = (−127 ± 22, 230 ± 54 km s^{-1}), (v_2, FWHM$_2$) = (10 ± 7, 45 ± 16 km s^{-1}), and (v_3, FWHM$_3$) = (130 ± 19, 174 ± 42 km s^{-1}). The integrated flux density of the CO(J = 2→1) emission line is (2.4 ± 0.7 Jy km s^{-1})/μ_{21}, where μ_{21} is the lensing magnification of the CO(J = 2→1) emitting region. Using the `uvmodelfit` task we independently estimate an average flux density of I = (3.4 ± 0.1 mJy)/μ_{21} within a spectral window of width 638 km s^{-1}.

6 LENSING ANALYSIS

We used the gravitational lens adaptive-mesh fitting code GLAFIC (Oguri 2010) to model the gravitational lens system HS 0810+2554. For modelling the source of the UV emission we assumed a point source. This assumption is justified by the estimated size of the UV accretion disc of HS 0810+2554 of $r_s \sim 3 \times 10^{15}$ cm ∼0.001 pc, assuming a black hole mass for HS 0810+2554 of

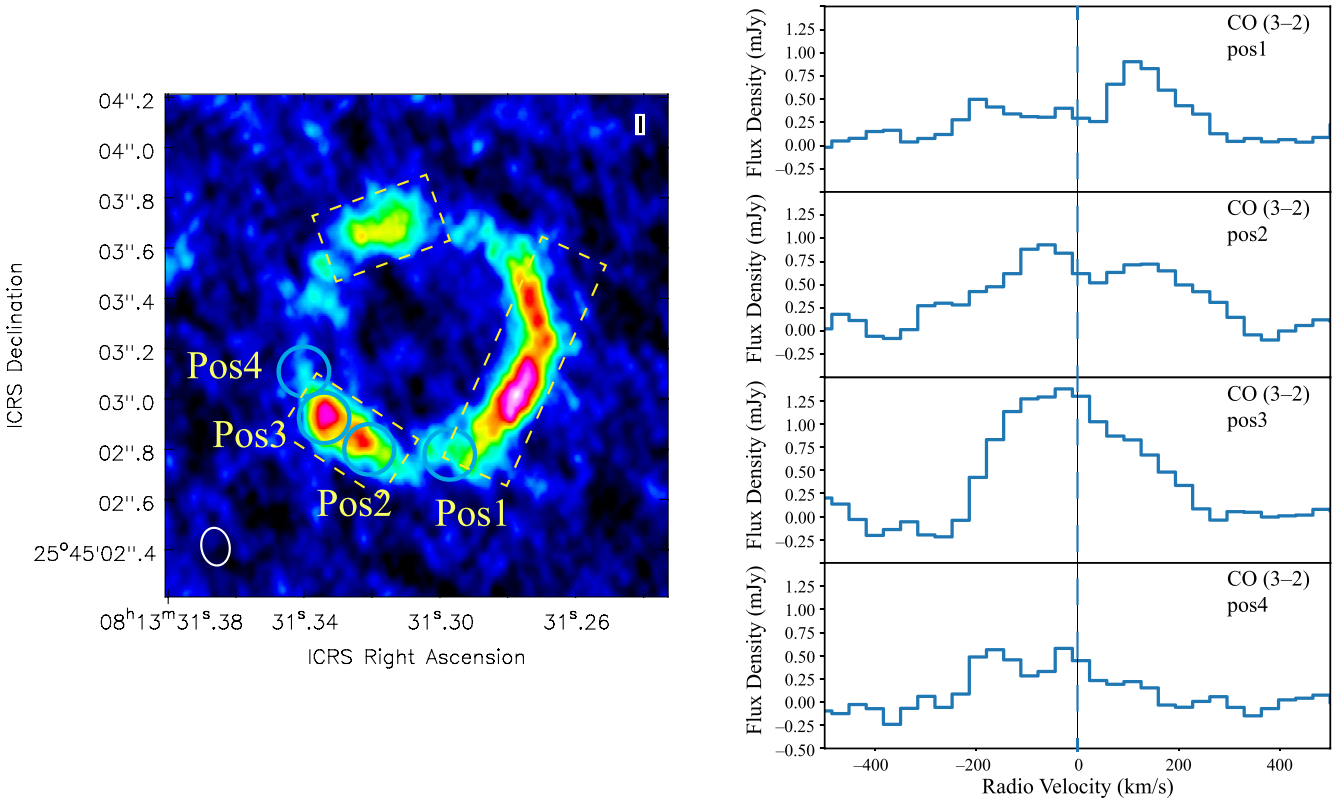

Figure 4. (Left) The image of HS 0810+2554 spectrally integrated over the CO(J = 3→2) line with solid circles representing the extraction regions used to produce the spectra on the right. (Right) CO(J = 3→2) spectra extracted from four different locations on the Einstein ring near image C. The observed Doppler shift is consistent with a rotating CO(J = 3→2) emission region. The dashed rectangular regions represent the three slices used to produce the position velocity diagrams shown in Fig. 5.

$M_{\rm BH} \sim (4.2 \pm 2.0) \times 10^8$ $M_\odot$ (e.g. Assef et al. 2011) and the $M_{\rm BH}$ versus $r_{\rm s}$ relation (fig. 9 of Morgan et al. 2018). The *HST* image of HS 0810+2554 does not show an Einstein ring in the UV band indicating that most of the observed UV emission most likely originates from the accretion disc. The parameters of the lens are constrained using the optical positions of the images obtained from *HST* observations of HS 0810+2554. The optical positions were taken from the CASTLES of gravitational lenses website http://cfa-www.harvard.edu/glensdata/. The lens is modelled with a singular isothermal ellipsoid (SIE) plus an external shear from the nearby galaxy group. The ellipsoid's orientation and ellipticity were left as free parameters. The magnification caustics with overlaid source and image positions are shown in Fig. 8.

In subsequent lens modelling of the ALMA observations we freeze the lens model parameters to the ones constrained from the *HST* observation. As shown in Fig. 1, the ALMA band 4 (1.96−2.19 mm) continuum emission shows a very different morphology than the *HST* ACS *F555W* image of HS 0810+2554. In particular, the ∼2 mm-continuum emission near images A and B is extended and not aligned with the optical emission and the ∼2 mm flux of image C is significantly lower than that of image D which is opposite to what is detected in the optical.

We first attempted to model the ALMA ∼ 2 mm-continuum emission with a point source, with its position set free in the source plane, assuming our best-fitting *HST* lens model. The fit with a point source model did not converge indicating that the observed ∼2 mm-continuum emission likely does not originate from a point-like source. We next model the ALMA ∼ 2 mm-continuum emission with an extended source in the form of an elliptical Gaussian of ellipticity e, position angle $\theta_{\rm e}$ and widths along the major and minor axes of σ_x and σ_y. As input to the modelling, we provide the ALMA high spatial resolution continuum moment 0 image via the GLAFIC command `readobs_extend` and optimize the lens modelling by including a circular mask region with a *radius* of 0.8 arcsec centred on the ALMA emission. Regions of the ALMA images within this masked region were used for optimization and those outside ignored. The GLAFIC command `readpsf` is used to read in the point spread function (PSF) produced by the CASA task `tclean`. The extended source images produced by GLAFIC are convolved with the PSF.

In Fig. 9, we show the ALMA ∼ 2 mm-continuum emission in the source plane and the corresponding lensed image of the ALMA ∼ 2 mm-continuum emission in the image plane. The best-fitting parameters of the extended continuum source model are presented in Table 3. For our assumed cosmology, the FWHM values of the best-fitting elliptical Gaussian source model to the 2 mm-continuum emission along the major and minor axes are ∼1.6 kpc and ∼365 pc, respectively. Assuming the ∼ 2 mm-continuum emission originates from an inclined circular disc, we use our source model to derive the disc inclination angle from the minor and major axial ratio (R) [i.e. $i = \cos^{-1}(R)$]. The estimated inclination angle of the continuum disc is $i_{\rm cont} \sim 77^\circ$. A second possibility is that the mm-continuum emission contains a jet component leading to the highly elongated morphology in the source plane shown in Fig. 9. VLBI observations of HS 0810+2554 at 1.75 GHz by Hartley et al. (2019) show a radio jet pointed in a similar direction in HS 0810+2554.

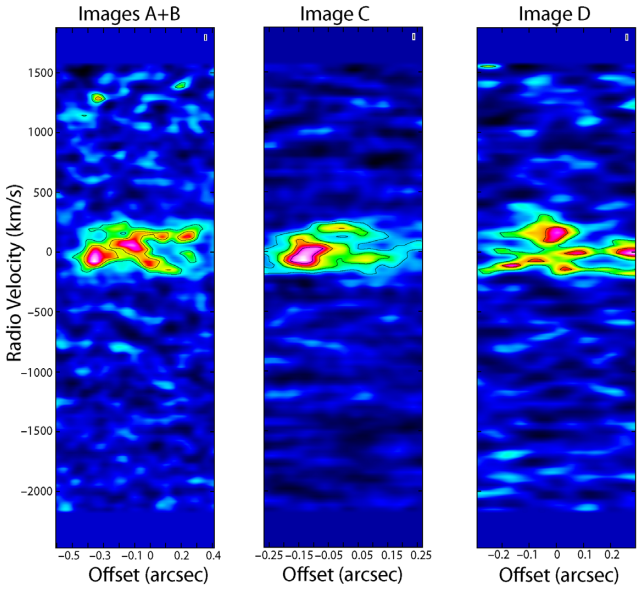

Figure 5. Position velocity diagrams for images A + B, C, and D of the high spatial resolution CO(J = 3→2) image cube of HS 0810+2554. The position velocity diagrams are computed over three slices in the direction plane centred on images A + B, C, and D (see Fig. 4). The start and endpoint positions of the slices correspond to negative and positive offsets following the Einstein ring along the clockwise direction. Contours overlaid correspond to [2, 3, 5, 7]σ for images A + B, [2, 3, 4, 5]σ for images C, and [2, 3, 4]σ for images D, where 1σ = 140 μJy beam^{-1}. Redshifted clumps with radio velocities of ∼1300 km s^{-1}are detected in the slice over images A + B (also see clump 1 in Fig. 12).

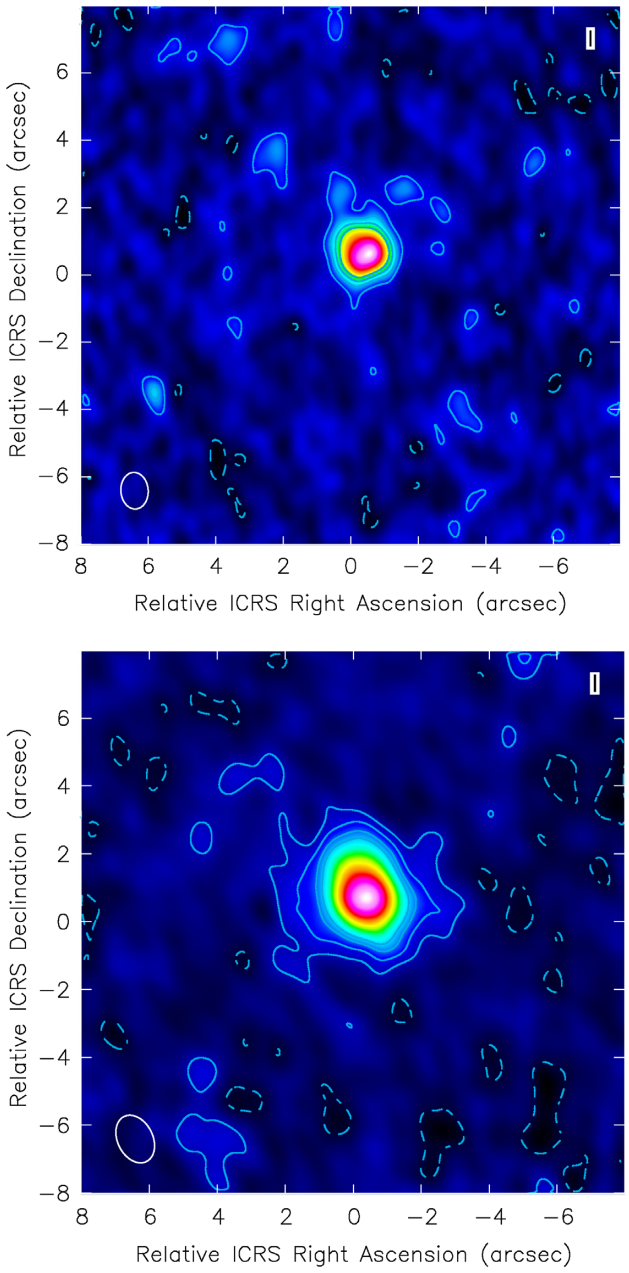

Figure 6. (Top) The ALMA CO(J = 2→1) moment 0 line emission of HS 0810+2554. Contours correspond to [−2, 2, 4, 6, 8]σ, where 1σ = 0.05 Jy beam^{-1} km s^{-1}. (bottom) The ALMA CO(J = 3→2) moment 0 line emission of HS 0810+2554 obtained with the ALMA compact configuration. Contours correspond to [−2, 2, 4, 6, 8]σ, where 1σ = 0.08 Jy beam^{-1} km s^{-1}.

Specifically, based on fig. 6 of Hartley et al. (2019), the position angle of the 1.75 GHz VLBI jet is $\theta = 61^{\circ}{}^{+10}_{-8}$, which is consistent with the position angle of $\theta_e \sim 65^{\circ}$ (see Table 3) of the lens-inverted ∼143 GHz continuum emission. We investigate the jet hypothesis further by determining the spectral index of the mm-continuum emission of HS 0810+2554. Typically, non-thermal synchrotron emission from jets dominates their SED at frequencies $\lesssim$10 GHz (Gioia, Gregorini & Klein 1982; Duric, Bourneuf & Gregory 1988; Zajaček et al. 2019) and thermal emission from dust in the disc begins to dominate at mm-wavelengths. The non-thermal synchrotron spectra of jets are often fit with power-law models of the form $S_\nu \propto \nu^\alpha$, where α is the spectral index. The best-fitting spectral index of the mm-continuum emission obtained from the ALMA observations of HS 0810+2554 is $\alpha = 2.8 \pm 0.3$ which is consistent with thermal emission and not pure synchrotron emission. We note, however, that strongly inverted spectra with $\alpha >$ 2 have been detected in the core of the jet in M87 (Zhao et al. 2019) and are thought to arise from synchrotron self-absorption and free–free absorption from an outflowing wind. In conclusion, the inverted spectral index of the mm-continuum emission does not support pure synchrotron emission as the origin of the elongated mm-continuum emission detected in the ALMA observations of HS 0810+2554. As we discuss in Section 8, the SED of HS 0810+2554 published in Stacey et al. (2018) is found to have a hot dust component suggesting that an AGN component may be contributing to the sub-mm and mm emission.

We next apply our lens model to the high-resolution CO(J = 3→2) line image of HS 0810+2554. As input to GLAFIC we provide the ALMA high spatial resolution CO(J = 3→2) moment 0 image and optimize the lens modelling by including a circular mask region with a radius of 0.8 arcsec centred on the ALMA emission. In Fig. 10, we show the ALMA CO(J = 3→2) emission in the source plane and the corresponding lensed image of the CO(J = 3→2) emission in the image plane. We note, however, that the morphology of the CO(J = 3→2) emission in the image and source plane differ in each frequency channel across the CO(J = 3→2) line. To account for the frequency dependence of the morphology of the CO(J = 3→2) emission and to illustrate the rotation of the CO(J = 3→2) region in the source plane, we perform a lens inversion to each frequency channel across the CO(J = 3→2) line of HS 0810+2554 shown in Fig. 2. Specifically, we first produce

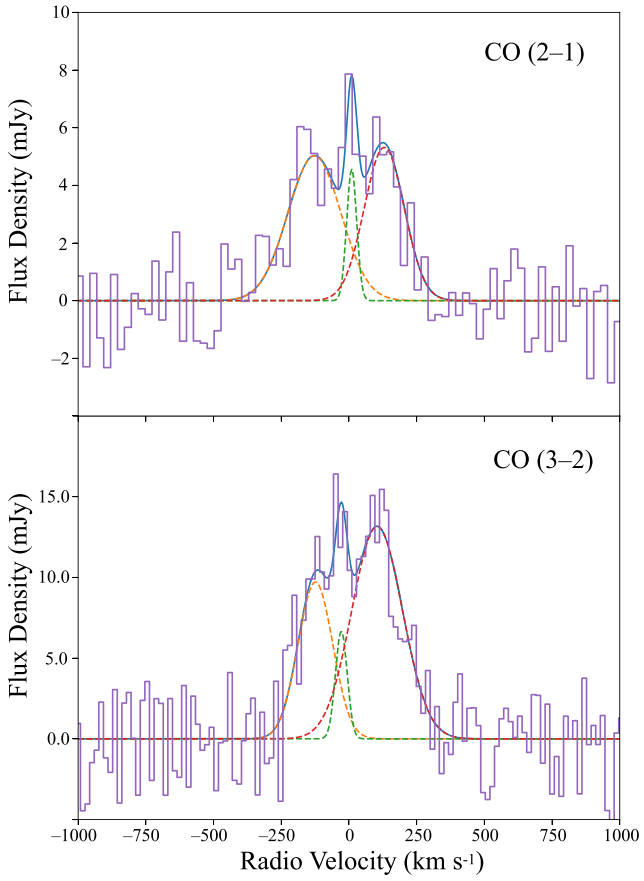

Figure 7. The ALMA CO(J = 3→2) and CO(J = 2→1) continuum-subtracted spectra of HS 0810+2554 obtained with the ALMA compact configuration. The spectral lines are fit with a model that consists of three Gaussians. The velocity shifts can be explained with the presence of a rotating molecular disc and are consistent with the best-fitting values derived from the CO(J = 3→2) spectrum obtained with the ALMA extended configuration.

images of the CO(J = 3→2) line emission at the 13 frequency channels between −180 and 230 km s^{-1}. We next use GLAFIC to model each one of the 13 images independently, assuming lens model parameters obtained from modelling the *HST* observation of HS 0810+2554 as described in Section 6. The extended source of the CO(J = 3→2) line emission in each frequency channel is modelled with an elliptical Gaussian of ellipticity e, position angle θ_e and widths along the major and minor axes of σ_x and σ_y, respectively. We create a spectral cube containing the reconstructed sources at each frequency channel. In Fig. 11, we show the derived moment 0 spectrally integrated map and the moment 1 velocity map of the CO(J = 3→2) line emission in the source plane. A clear rotation is seen in the moment 1 map, with the north(south) portions of the CO(J = 3→2) emission moving towards (away from) us. The FWHM values of the best-fitting elliptical Gaussian source model to the CO(J = 3→2) emission along the major and minor axes are ∼950 and ∼690 pc, respectively. Assuming the CO(J = 3→2) line emission originates from an inclined circular disc, our source model implies an inclination angle of the CO(J = 3→2) disc of $i_{CO(3-2)} \sim 43°$.

We invoke the *writelens* command in GLAFIC to obtain various lensing properties including the magnification map $\mu(i, j)$ of the lens. We use this magnification map to estimate the total magnification of the mm-continuum and line emission of HS 0810+2554 detected in the ALMA observations. Specifically, for an observed intensity distribution of $I(i, j)$, the total magnification of the extended source will be

$$\mu_{\rm tot} = \frac{\sum I\,(i\,,\,j)}{\sum \frac{I(i,j)}{\mu(i,j)}}. \quad (1)$$

We find the total magnifications of the mm-continuum and the CO(J = 3→2) emission to be $\mu_{\rm cont} \sim 7 \pm 3$ and $\mu_{\rm CO(3-2)} \sim 10 \pm 2$, respectively. The calculations of the total magnifications were based on the high spatial resolution observations. The uncertainty of the magnifications were estimated by considering emission lying within the 2σ and 2.5σ confidence levels.

Our lensing analysis indicates that the centroids of the extended mm (continuum and line emission) and point-like UV source emission regions are separated by about 0.035 arcsec, corresponding to ∼300 pc for our assumed cosmology (see Figs 9–11). One

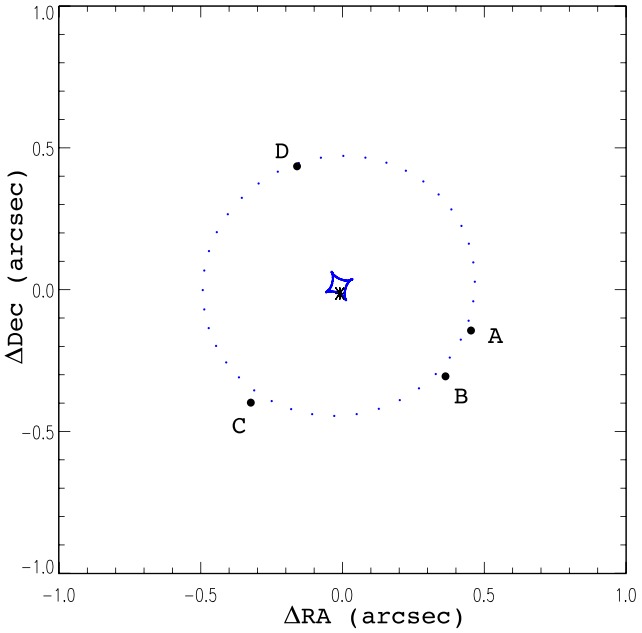

Figure 8. Results from lens modelling the *HST* observation of HS 0810+2554. The lens model reproduces the observed *HST* image positions. This best-fitting lens model is used for subsequent lensing analysis of the ALMA observations. The tangential critical curve is represented by the dotted line, the caustic by the solid line and the UV point source in the source plane with an asterisk.

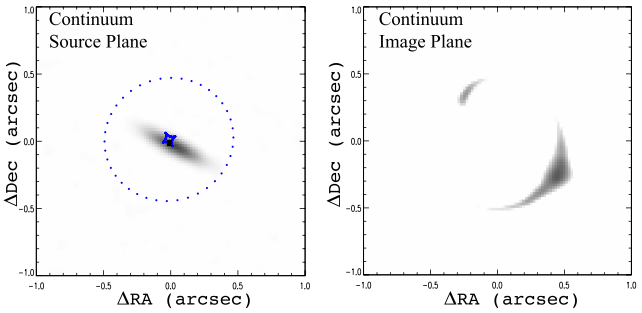

Figure 9. Results from lens modelling the ∼2 mm-continuum emission of HS 0810+2554. (Left) The ∼2 mm-continuum emission in the source plane. (Right) The ∼2 mm-continuum emission in the image plane.

Table 3. Results of lens modelling of 2 mm-continuum and CO(J = 3→2) emission of HS 0810+2554.

Source[a]	x_c	y_c	e^b	$\theta_e{}^c$	$\sigma_x{}^d$	$\sigma_y{}^d$
	(arcsec)	(arcsec)		(°)	(arcsec)	(arcsec)
2 mm-continuum	4×10^{-3}	-8×10^{-3}	0.97	65	0.079	0.018
CO(J = 3→2)	3×10^{-2}	-2×10^{-2}	0.69	110	0.047	0.034

[a]The moment 0 images of the 2 mm-continuum and CO(J = 3→2) line lensed emission observed in the high spatial resolution observation are modelled assuming extended sources having an elliptical Gaussian geometry.
[b]The ellipticity of the source emission.
[c]The position angle of the source emission.
[d]σ_x and σ_y represent the widths of the Gaussians along the major and minor axes, respectively. The FWHM values are 2.3548σ.

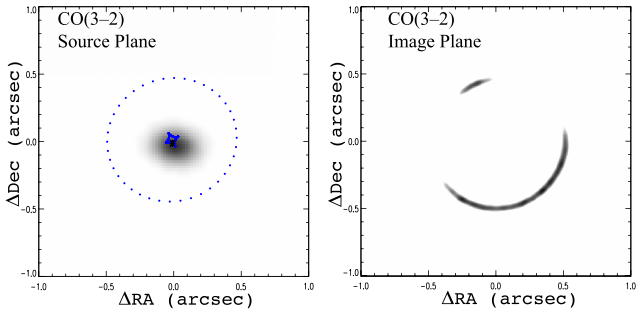

Figure 10. Results from lens modelling the CO(J = 3→2) line emission of HS 0810+2554. (Left) The CO(J = 3→2) line emission in the source plane. (Right) The CO(J = 3→2) line emission in the image plane.

possible explanation for this offset is that a portion of the extended mm emission is obscured along our line of sight. We caution, however, that higher S/N ALMA images would be required to confirm this offset.

7 POSSIBLE DETECTION OF HIGHLY BLUESHIFTED AND REDSHIFTED CLUMPS OF CO(J = 3→2) EMISSION

We have identified 10 blueshifted/redshifted emission lines that are associated with nine clumps of mm emission. Given the relatively high velocities observed ($\gtrsim$1000 km s^{-1}), it is unlikely that the redshifted emission is produced by the Doppler shift of infalling gas from the near side of the CO gas. A more likely scenario is that the blueshifted (redshifted) emission is produced by the Doppler shift of outflowing material from the near(far) side of the CO gas. In the left-hand panels of Fig. 12, we show the images of HS 0810+2554 spectrally integrated over the frequencies within the blueshifted or redshifted emission lines associated with clumps overlaid on the moment 0 CO(J = 3→2) contour map. On the right-hand panels of Fig. 12, we show the mm spectra extracted from circular regions of radii ∼0.1 arcsec centred on the clumps. The properties and significance of the blueshifted and redshifted emission lines were determined by fitting them with Gaussians and calculating the integrated rms of the background under each line. The significance of the lines detected lie in the range of 3.0–4.7σ and the velocities lie between −1702 and +1304 km s^{-1}. In Table 4, we list the positions, velocities with respect to systemic, FWHM, integrated flux densities with 1σ errors, detection significance, lensing magnifications, distances from the centre of the galaxy

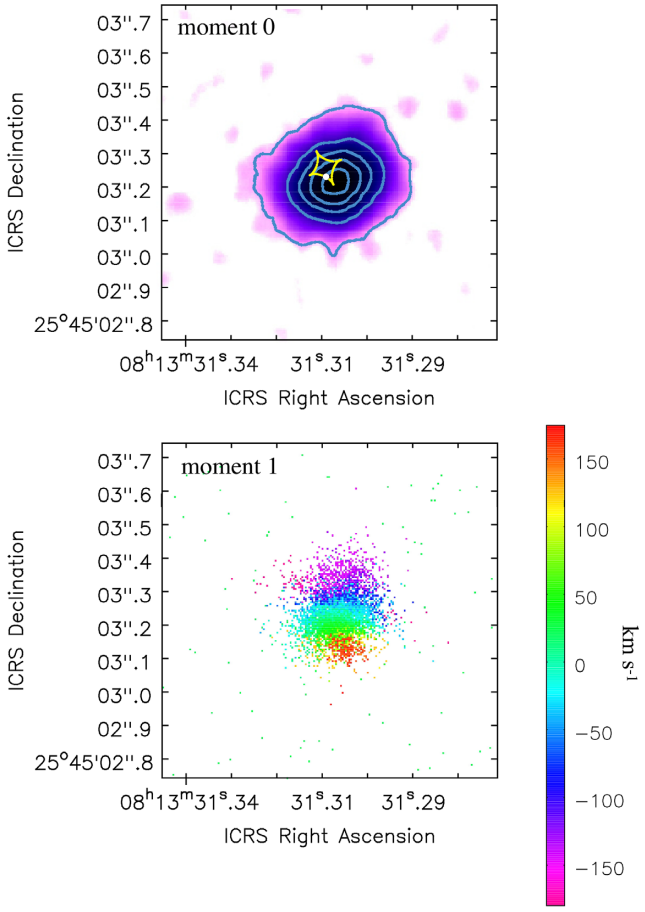

Figure 11. (Top) The CO(J = 3→2) moment 0 line emission in the source plane, derived from a lens inversion to each frequency channel across the CO(J = 3→2) line (see the text for details). Contours correspond to 0.9, 0.7, 0.5, 0.3, and 0.1 of the peak. The UV point source in the source plane is represented with a solid white circle. (bottom) The moment 1 velocity map of the CO(J = 3→2) line emission of HS 0810+2554 calculated in the source plane. A clear rotation is seen, with the north(south) portions of the CO(J = 3→2) emission moving towards (away from) us. The rotation is consistent with the spectrum of HS 0810+2554 shown in Fig. 2.

and total masses of the clumps. In Fig. 13, we show the spatial distribution of all the clumps overplotted on the CO(J = 3→2) moment 0 line emission of HS 0810+2554. We note that clump 1

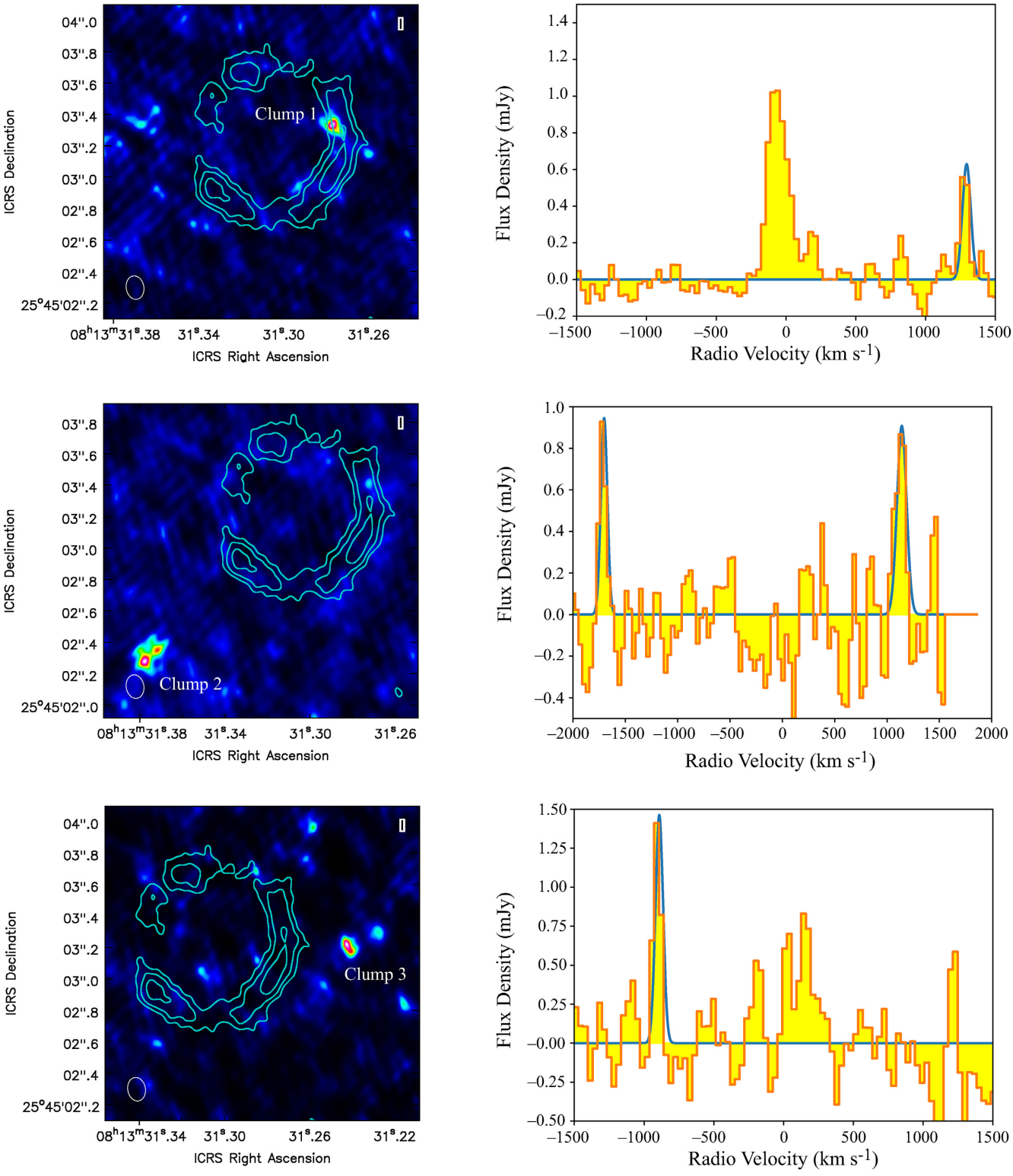

Figure 12. Possible blueshifted and redshifted CO(J = 3→2) emission lines associated with clumps. (Left) Images of HS 0810+2554 spectrally integrated over the frequencies within the blueshifted or redshifted emission lines associated with clumps overlaid on the moment 0 CO(J = 3→2) contour map. (Right) The ALMA mm spectra extracted from circular regions of radii ∼0.1 arcsec centred on the clumps. The best-fitting Gaussian-line models are overplotted on the spectra.

Table 4. Properties of redshifted and blueshifted clumps of CO(J = 3→2) emission.

Clump[a]	RA	Dec.	$v_{\rm offset}$ (km s^{-1})	FWHM (km s^{-1})	$F_{\rm d}$[b] (Jy km s^{-1})	S/N σ	μ[c]	$r_{\rm clump}$[d] (kpc)	$M_{\rm clump}$ ($\times 10^8$ M$_\odot$)	$\dot{M}_{\rm clump}$ (M$_\odot$ yr^{-1})
1	8:13:31.277	+25:45:3.335	1294 ± 12	71 ± 28	0.047 ± 0.010	4.7	18.3	0.95 ± 0.1	0.28 ± 0.07	39 ± 10
2	8:13:31.370	+25:45:2.415	1141 ± 10	107 ± 22	0.101 ± 0.033	3.1	1.7	10.9 ± 0.1	6.5 ± 2.1	70 ± 23
2	8:13:31.370	+25:45:2.415	−1702 ± 8	73 ± 18	0.074 ± 0.023	3.2	1.7	10.9 ± 0.1	4.7 ± 1.9	75 ± 34
3	8:13:31.241	+25:45:3.194	−890 ± 6	64 ± 14	0.070 ± 0.023	3.1	2.2	7.5 ± 0.1	3.5 ± 1.5	43 ± 18
4	8:13:31.440	+25:45:0.864	1018 ± 7	95 ± 17	0.101 ± 0.033	3.0	1.3	25.7 ± 0.1	8.5 ± 2.4	34 ± 10
5	8:13:31.424	+25:45:2.107	−891 ± 6	64 ± 13	0.098 ± 0.023	4.3	1.4	16.7 ± 0.1	7.6 ± 1.8	41 ± 10
6	8:13:31.332	+25:45:2.141	1267 ± 6	81 ± 15	0.053 ± 0.016	3.3	1.8	9.9 ± 0.1	3.2 ± 0.9	42 ± 12
7	8:13:31.273	+25:45:1.171	1304 ± 9	109 ± 20	0.058 ± 0.016	3.5	1.4	18.3 ± 0.1	4.5 ± 1.2	33 ± 9
8	8:13:31.214	+25:45:3.503	−727 ± 7	78 ± 17	0.042 ± 0.011	3.2	1.6	11.0 ± 0.1	2.9 ± 0.8	20 ± 5
9	8:13:31.201	+25:45:0.852	−868 ± 7	73 ± 16	0.024 ± 0.006	3.9	1.3	24.0 ± 0.1	2.0 ± 0.6	7 ± 2

[a]The clumps of CO(J = 3→2) emission are shown in Fig. 12. Clump 2 shows both a redshifted and blueshifted component.
[b]Integrated flux densities are not corrected for magnification.
[c]The magnifications at the locations of the clumps were calculated from the magnification map of HS 0810+2554 described in Section 6.
[d]Clump 1 is located on the CO(J = 3→2) Einstein ring and based on our lens inversion is estimated to be at a distance of about 0.7 pc from the AGN. For our assumed cosmology, the scale at $z = 1.51$ is 8.6 kpc arcsec^{-1}.

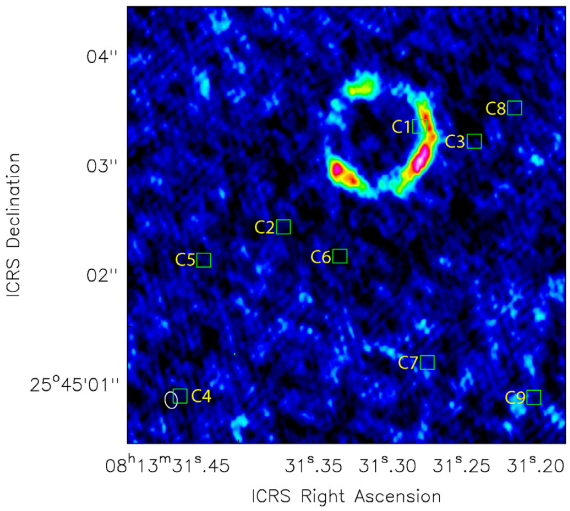

Figure 13. The CO(J = 3→2) moment 0 line emission of HS 0810+2554 with the locations of all the clumps centred on the labelled boxes. The ALMA pointing was centred on the centre of this image and the maximum recoverable scale (MRS) in the ALMA extended configuration is MRS = 1.7 arcsec.

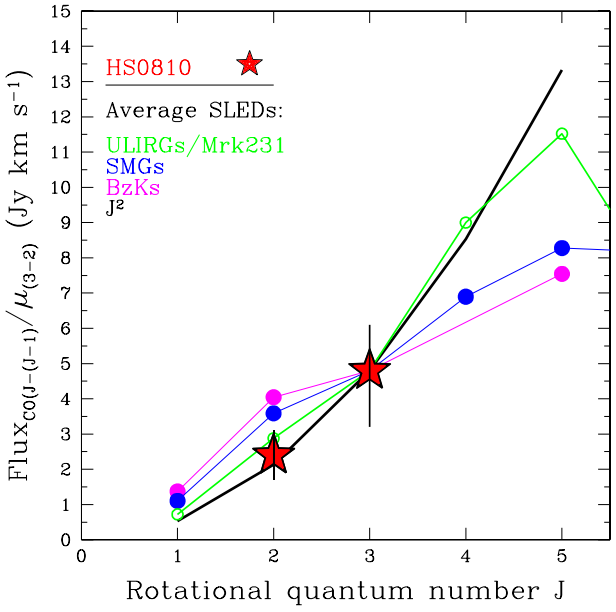

Figure 14. CO excitation ladder of HS 0810+2554 (stars) compared with average SLED values obtained for various classes of sources (SMGs, ULIRGs, BzKs, as labelled; taken from Papadopoulos et al. 2012; Bothwell et al. 2013; Daddi et al. 2015), for Mrk 231 (from Fixsen et al. 1999; van der Werf et al. 2010). The black curve show the J^2 trend (e.g. LTE assumption). All CO SLEDs are normalized to the CO(J = 3→2) flux observed in HS 0810+2554.

is also clearly visible in the pv diagram extracted along the A + B images and shown in Fig. 12.

8 DISCUSSION AND CONCLUSIONS

We have presented results from the spectral and spatial analysis of ALMA observations of the $z = 1.51$ lensed quasar HS 0810+2554. Several important properties of the molecular gas in the host galaxy can be inferred from these results. Specifically, we are able to estimate both the total mass of the molecular gas and the energetics of the possible outflows associated with possible high-velocity clumps of molecular gas detected in HS 0810+2554.

In Section 5, we show that the integrated flux density of the CO(J = 2→1) and CO(J = 3→2) emission of HS 0810+2554 are 2.4 ± 0.7 Jy km s^{-1}/μ_{21} and 4.8 ± 1.3 Jy km s^{-1}/μ_{32}, respectively. Fig. 14 shows the CO Spectral Line Energy Distribution (SLED) of HS 0810+2554 based on these two values and compared to several CO SLEDs of different classes of high-z and ultraluminous galaxies. The ratio of the CO(J = 3→2) to CO(J = 2→1) emissions measured from our ALMA data shows that the CO SLED of HS 0810+2554 is consistent with a J^2 dependence applicable to bright QSOs from Carilli & Walter (2013). Our lensing analysis in Section 6 describes our method for estimating the magnification factors $\mu_{32} = 10 \pm 2$ and $\mu_{\rm cont} = 7 \pm 3$. Assuming the geometries of the CO(J = 2→1)/μ_{21} and CO(J = 3→2)/μ_{32} emission regions are similar we adopt $\mu_{32} = \mu_{21}$.

The CO line luminosity can be expressed as

$$L_{\rm CO} = 2453 S_{\rm CO} \Delta v D_{\rm L}^2 (1+z)^{-1}, \quad (2)$$

where $S_{CO}\Delta v$ is the integrated flux density of the CO(J = 1→0) line. Assuming magnifications of $\mu_{32} = \mu_{21} = 10 \pm 2$, and $S_{CO(3-2)}\Delta v/S_{CO(1-0)}\Delta v = 9$ (see Fig. 14), we find $L_{CO} = (6.6 \pm 1.9)/\mu_{32} \times 10^{10}$ K km s^{-1} pc^2.

Following Solomon & Vanden Bout (2005), the total mass of the molecular gas is expressed as

$$M_{Mol} = \alpha_{CO} L_{CO}, \quad (3)$$

where M_{Mol} is in units of $M_\odot$, L_{CO} is in units of K km s^{-1} pc^2, and α_{CO} is the CO-to-H_2 conversion factor. Assuming a ULIRG-like CO-to-H_2 conversion factor of $\alpha_{CO} = 0.8\ M_\odot$ (K km s^{-1} pc^2)$^{-1}$, we find that the total gas mass of the molecular gas in HS 0810+2554 to be $M_{Mol} = (5.2 \pm 1.5)/\mu_{32} \times 10^{10}\ M_\odot$.

Stacey et al. (2018) note that the high effective dust temperature of ∼89 K of HS 0810+2554 may be the result of a significant contribution from the AGN heating the dust in addition to heating provided by star formation. By modelling the FIR dust emission with a two-temperature model, Stacey et al. derive an FIR luminosity of $3.7^{+1.7}_{-2.3} \times 10^{12}\ L_\odot/\mu_{FIR}$ for the cold component that likely originates from star formation. Assuming the FIR luminosity of the cold component is produced by star formation, we derive a star formation rate (SFR) for HS 0810+2554 of SFR $= 640^{+400}_{-300}/\mu_{FIR}\ M_\odot\ yr^{-1}$ (Kennicutt 1998). We estimate the molecular gas depletion time, defined as

$$\tau_{dep}^{mol} = \frac{\Sigma_{mol}}{\Sigma_{SFR}} \quad (4)$$

to be $\tau_{dep}^{mol} \sim 8.2 \times 10^7\ (\mu_{FIR}/\mu_{32})$ yr, where Σ_{mol} and Σ_{SFR} are the surface densities of molecular gas and star formation, respectively.

Assuming the CO(J = 3→2) line emission originates from an inclined rotating circular disc, we estimate the dynamical mass of this disc from the relation $M_{dyn} = 1.16 \times 10^5\ v_{cir}^2 D\ M_\odot$, where D is the disc diameter in kpc and v_{cir} is the maximum circular velocity of the CO(J = 3→2) disc in km s^{-1} (Wang et al. 2013). v_{cir} is approximated as $v_{cir} = 0.75 FWHM_{CO(3-2)}/\sin i$, where i is the inclination angle of the disc. We estimate the dynamical mass within the CO(J = 3→2) disc to be $M_{dyn} = (3.2 \pm 0.4) \times 10^{10}\ M_\odot$.

In Table 4, we also provide estimates of the mass outflow rates associated with the redshifted and blueshifted clumps. The masses in the clumps range from 0.3×10^8 to $8 \times 10^8\ M_\odot$ (of the order of few per cent of the total gas mass).

Assuming that the blueshifted and redshifted clumps are associated with outflows, we provide an estimate of the outflow rates averaged over the wind lifetime of the detected clumps based on the equation (Rupke & Veilleux 2005):

$$\dot{M} = \frac{M_{clump} v_{clump}}{r_{clump}}. \quad (5)$$

This equation assumes that the clumps have been moving at the observed velocity of v_{clump} for their lifetime. We note that r_{clump} in this equation is the distance of a clump from the AGN, whereas, we observe projected distances. Our estimates of the total mass of the molecular gas and the mass inflow and outflow rates of HS 0810+2554 are used to determine the dynamical time, t_{dyn}, in which the gas can be depleted. Specifically, t_{dyn} is derived from the expression

$$t_{dyn} \approx \frac{M_{Mol}}{\dot{M}_{Outflow}}. \quad (6)$$

We find a dynamical depletion time of $t_{dyn} = (1.3 \pm 0.4)/\mu_{32} \times 10^8$ yr.

The rate of change of momentum of the molecular outflow is $\dot{p}_{mo} = \dot{M} v_{clump}$ and the momentum boost is $\dot{p}_{mo}/(L_{Bol}/c)$. The bolometric luminosity, $\log(L_{Bol}/\text{erg s}^{-1}) = 45.54$ (corrected for magnification of $\mu = 103$), is provided from the monochromatic luminosity of HS 0810+2554 at 1450 Å, $\log(\lambda L_\lambda/\text{erg s}^{-1}) = 45.04$, based on the empirical equations of Runnoe et al. (2012). The UV monochromatic luminosity density of HS 0810+2554 at 1450 Å was obtained from analysing its available SDSS spectrum.

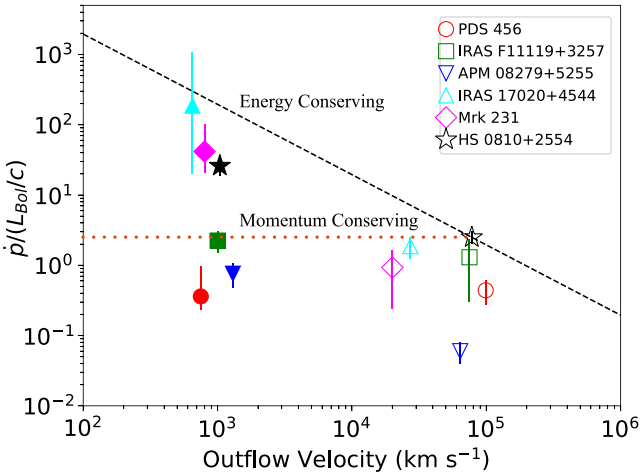

Figure 15. The momentum boost $\dot{p}/(L_{Bol}/c)$ as a function of outflow velocity. The filled and unfilled symbols correspond to the molecular and UFOs, respectively. The dashed and dotted lines represent the dependence of the momentum boost with outflow velocity for energy-conserving and momentum-conserving outflows, respectively for HS 0810+2554. The data for AGNs other than HS 0810+2554 have been obtained from the literature (e.g. Feruglio et al. 2015, 2017; Tombesi et al. 2015; Veilleux et al. 2017; Bischetti et al. 2019). For consistency, we have adjusted published results assuming the same conversion factor of $\alpha_{CO} = 0.8\ M_\odot$ (K km s^{-1} pc^2)$^{-1}$ for estimating the total molecular gas mass.

In Fig. 15, we show the momentum boost $\dot{p}/(L_{Bol}/c)$ plotted against the outflow velocity for HS 0810+2554 based on this work. The $(\dot{p}_{xo}/(L_{Bol}/c), v_{xo})$ values for the two components of the UFO of HS 0810+2554 obtained from the observation on 2014 October 4 are $(1.5 \pm 0.4, 0.12 \pm 0.04c)$ and $(1.0 \pm 0.2, 0.42 \pm 0.04\ c)$. The combined momentum boost and the average outflow velocity of the UFO of HS 0810+2554 are shown in Fig. 15. Based on our analysis the $(\dot{p}_{mo}/(L_{Bol}/c), v_{mo})$ values of the molecular outflow are $(26 \pm 6, 1040$ km s$^{-1})$. The momentum boost of the molecular outflow of HS 0810+2554 is calculated by combining the nine outflowing clumps listed in Table 4 and the outflow velocity represents the average of the clump velocities. The momentum boost of the outer molecular wind of HS 0810+2554 is slightly below the value expected for an energy-conserving outflow, given the observed UFO momentum boost.

In Fig. 15, we also show the momentum boosts and velocities of the ultrafast and molecular outflows of several other AGNs based on published results. Specifically, estimates for PDS 456 are from Boissay-Malaquin et al. (2019) and Bischetti et al. (2019), estimates for IRAS F11119+3257 are based on Tombesi et al. (2015) and Veilleux et al. (2017), estimates for APM 08279+5255 are based on Feruglio et al. (2017), estimates for IRAS 17020+4544 are from Longinotti et al. (2018), estimates for Mrk 231 are from Feruglio et al. (2015), and estimates for HS 0810+2554 are based on Chartas et al. (2016) and this study. For consistency we have adjusted published results assuming the same conversion factor of $\alpha_{CO} = 0.8\ M_\odot$ (K km s^{-1} pc^2)$^{-1}$ for estimating the total molecular gas mass. The two AGNs of this small sample that have

momentum boosts consistent with a momentum-conserving outflow are PDS 456 and IRAS F11119+3257, whereas the other objects including HS 0810+2554 are closer to having energy-conserving outflows. Smith et al. (2019) find a similar result in the sense that the efficiency factors coupling the small-scale relativistic winds and the large-scale molecular outflows of their sample of objects varies significantly.

Mizumoto et al. (2019) reported several trends between the energy-transfer rate C defined as

$$C = \frac{\frac{1}{2}\dot{M}_{\rm mol} v_{\rm mol}^2}{\frac{1}{2}\dot{M}_{\rm UFO} v_{\rm UFO}^2} \quad (7)$$

and AGN properties such as black hole mass $M_{\rm BH}$ and $L_{\rm Bol}/L_{\rm Edd}$. We calculate the energy-transfer rate of HS 0810+2554 to be $C = 0.2 \pm 0.1$ with $L_{\rm Bol}/L_{\rm Edd} = 0.07 \pm 0.03$. We find that HS 0810+2554 is only marginally consistent, within the error bars, with the C versus $M_{\rm BH}$ and C versus $L_{\rm Bol}/L_{\rm Edd}$ trends reported in Mizumoto et al. (2019). We estimated the strength of the proposed $M_{\rm BH}$ versus C and $L_{\rm Bol}/L_{\rm Edd}$ versus C trends before and after adding the data from HS 0810+2554. Before including HS 0810+2554 to the Mizumoto et al. (2019) sample, we find that the Kendall's rank correlation coefficient, τ and its significance are $\tau = -0.33$ significant at $>$ 71 per cent confidence for the C versus $M_{\rm BH}$ data and $\tau = 0.62$ significant at $>$ 95 per cent confidence for the $L_{\rm Bol}/L_{\rm Edd}$ versus C data. Including HS 0810+2554 to the Mizumoto et al. 2019 sample, we find $\tau = -0.21$ significant at $>$54 per cent confidence for the C versus $M_{\rm BH}$ data and $\tau = 0.57$ significant at $>$95 per cent confidence for the C versus $L_{\rm Bol}/L_{\rm Edd}$ data. In conclusion, we find no significant trend of the energy-transfer rate versus $M_{\rm BH}$, whereas we confirm that the trend of the energy-transfer rate versus $L_{\rm Bol}/L_{\rm Edd}$ is significant at the $>$95 per cent confidence level.

There are significant limitations in using single epoch momentum boost estimates of molecular and UFOs to infer whether a flow is energy or momentum conserving. We are currently observing the energetics of the macro-scale molecular outflows that were possibly driven by micro-scale UFOs produced a considerable time earlier. According to several theoretical models (e.g. Faucher-Giguère & Quataert 2012; Zubovas & King 2012), UFOs are thought to interact with the ISM and then slow down to a speed of $\sim$1000 km s^{-1} and travel at this speed through the galaxy. The time for these slow molecular outflows to travel a distance of $\sim$1–10 kpc (observed distances of molecular outflows) is 10^6–10^7 yr. It is therefore possible that the energetics of the UFOs have varied significantly over the past 10^6–10^7 yr time frame making the comparison of the energetics of the micro- and macro-scale outflows difficult. Another important issue is that part of the energy of the micro-scale UFO may have been channelled to drive ionized gas which has not been included in this analysis.

The main conclusions of our spectral and spatial analyses of the ALMA observations of HS 0810+2554 are the following:

(i) The mm-continuum emission of HS 0810+2554 is detected and resolved with ALMA. The flux density of the continuum of the combined images at a mean frequency of 143 GHz is estimated to be $(401 \pm 50\ \mu{\rm Jy})/\mu_{\rm cont}$, where $\mu_{\rm cont} = 7 \pm 3$ is our estimated lensing magnification of the continuum. The positions, flux densities, and significances of the resolved lensed images are listed in Table 2.

(ii) The CO(J = 2→1) and CO(J = 3→2) line emissions of HS 0810+2554 are detected with ALMA. The CO(J = 3→2) line emission was observed with the ALMA extended configuration (beam size 0.1 arcsec × 0.06 arcsec) revealing a spectacular Einstein ring (see Fig. 3). The integrated flux density of the CO(J = 3→2) emission line is $(4.8 \pm 1.3$ Jy km s$^{-1})/\mu_{32}$, where $\mu_{32} = 10 \pm 2$. The integrated flux density of the CO(J = 2→1) emission line is $(2.4 \pm 0.7$ Jy km s$^{-1})/\mu_{21}$, where $\mu_{21} = 10 \pm 2$. Assuming a ratio of CO(J = 3→2)/CO(J = 1→0) $\sim$9 based on CO-SLED model for quasars and for an $\alpha_{\rm CO} = 0.8$ M$_\odot$ (K km s^{-1} pc^2)$^{-1}$ we estimate the molecular gas mass of HS 0810+2554 to be $M_{\rm Mol} = (5.2 \pm 1.5)/\mu_{32} \times 10^{10}$ M$_\odot$. We estimate the dynamical mass of the CO(J = 3→2) disc to be $M_{\rm dyn} = (3.2 \pm 0.4) \times 10^{10}$ M$_\odot$.

(iii) We find a significant offset between the positions of the lensed images of HS 0810+2554 as observed in the mm-continuum band and the image positions in the optical (see Fig. 1). An offset is also detected between the lensed images observed in the mm-continuum band and the Einstein ring that is resolved in the CO(J = 3→2) line (see Fig. 3). Our lens modelling of HS 0810+2554 indicates that the image offset is caused by the different morphologies of the mm-continuum and CO(J = 3→2) line emission regions. Specifically, based on our lens modelling, we find the FWHM values of the best-fitting elliptical Gaussian source model to the 2 mm-continuum emission along the major and minor axes are $\sim$1.6 kpc and $\sim$365 pc, respectively. We caution that our constrained values for the size of the extended continuum emission is very uncertain due to the assumed simplistic elliptical source model, the low S/N of the continuum ALMA data and the inherent problems with lens modelling the synthesized ALMA data. Higher S/N ALMA images of the continuum will be required before a more detailed lensing analysis can be performed to better constrain the source morphology and provide insight into the origin of the $\sim$2 mm-continuum source emission. The FWHM values of the best-fitting elliptical Gaussian source model to the CO(J = 3→2) emission along the major and minor axes are $\sim$950 and $\sim$690 pc, respectively. Assuming the $\sim$2 mm-continuum and CO(J = 3→2) emission originate from inclined circular discs, our source models imply an inclination angle of the continuum disc of $i_{\rm cont} \sim 77^\circ$ and of the CO(J = 3→2) disc of $i_{\rm CO(3-2)} \sim 43^\circ$. We investigated a second possibility that the continuum emission contains a jet leading to the highly elongated morphology in the source plane shown in Fig. 9. VLBI observations at 1.75 GHz by Hartley et al. (2019) find a radio jet pointed in a similar direction in HS 0810+2554. The inverted spectral index of $\alpha = 2.8 \pm 0.3$ of the mm-continuum emission of HS 0810+2554, however, does not support pure synchrotron emission as the origin of the elongated mm-continuum emission.

(iv) The CO(J = 2→1) and CO(J = 3→2) line spectra of HS 0810+2554 obtained with the ALMA compact configuration are broad and appear to contain three dominant peaks. The two outer peaks of the CO(J = 2→1) and CO(J = 3→2) lines are separated by $\Delta v_{21} = 257 \pm 29$ km s^{-1} and $\Delta v_{32} = 228 \pm 27$ km s^{-1}, respectively. The CO(J = 3→2) line spectrum of the high spatial resolution data set also contains three dominant peaks with the two outer peaks separated by $\Delta v_{32} = 254 \pm 23$ km s^{-1}. These velocity shifts imply the presence of a rotating molecular disc. A rotating molecular disc is supported by the detected shift of the CO(J = 3→2) spectrum as a circular spectral extraction region is shifted across the stretched image of the extended line emission (see Fig. 4). Our reconstruction of the CO(J = 3→2) source emission in multiple radio velocities clearly shows the rotation of the molecular gas (see Fig. 11).

(v) We report the possible detection of highly redshifted and blueshifted clumps of CO(J = 3→2) emission. We assume that the blueshifted (redshifted) emission is produced by the Doppler shift of outflowing material from the near(far) side of the CO gas.

The significance of the detections of the clumps ranges from 3σ to 4.7σ, the velocities range from -1702 to 1304 km s^{-1} and the estimated mass outflow rates range from $\sim$7 to $\sim$75 M$_\odot$ yr^{-1}. We estimate the dynamical depletion time of the molecular gas to be $t_{\rm dyn} = (1.3 \pm 0.4)/\mu_{32} \times 10^8$ yr. This time does not include possible depletion of gas due to star formation.

(vi) We would like to point out that while in the local Universe ($z \lesssim 0.2$) the number of objects with simultaneous detection of UFOs and molecular outflows is approaching $\sim$10 (see Mizumoto et al. 2019; Smith et al. 2019), HS 0810+2554 is the only other object at $z > 1$ in addition to APM 08279+5255 where a simultaneous detection has been made. We estimate the momentum boost, $\dot{p}_{\rm mo}/(L_{\rm Bol}/c)$, of the possible molecular outflow of HS 0810+2554 to be 26 ± 6. The momentum boost of the molecular wind of HS 0810+2554 is slightly below the value predicted for an energy-conserving outflow given the momentum flux observed in the UFO. We caution that the significance of several of the blueshifted and redshifted clump detections are relatively low and a deeper ALMA observation of HS 0810+2554 would be required to confirm these results.

(vii) Mizumoto et al. (2019) reported trends between the energy-transfer rate C and the black hole mass $M_{\rm BH}$ and $L_{\rm Bol}/L_{\rm Edd}$. With and without including HS 0810+2554 to the Mizumoto et al. (2019) sample we find no significant trend of the energy-transfer rate versus $M_{\rm BH}$, whereas we confirm that the trend of the energy-transfer rate versus $L_{\rm Bol}/L_{\rm Edd}$ is significant at the $>$ 95 per cent confidence level.

ACKNOWLEDGEMENTS

We acknowledge financial support from PRIN MIUR 2017PH3WAT ('Black hole winds and the baryon life cycle of galaxies'). GC would like to express his profound appreciation to the gracious faculty and staff of the Dipartimento di Fisica e Astronomia dell'Università degli Studi di Bologna and INAF/OAS of Bologna for their enduring collaboration and generous hospitality in providing a stimulating environment during his visits to their esteemed institutions. We greatly appreciate the useful comments made by the referee. This paper makes use of the following ALMA data: ADS/JAO.ALMA#2017.1.01368.S. ALMA is a partnership of ESO (representing its member states), NSF (USA), and NINS (Japan), together with NRC (Canada), MOST and ASIAA (Taiwan), and KASI (Republic of Korea), in cooperation with the Republic of Chile. The Joint ALMA Observatory is operated by ESO, AUI/NRAO, and NAOJ. The National Radio Astronomy Observatory is a facility of the National Science Foundation operated under cooperative agreement by Associated Universities, Inc.

REFERENCES

Assef R. J. et al., 2011, ApJ, 742, 93
Bischetti M. et al., 2019, A&A, 628, A118
Boissay-Malaquin R., Danehkar A., Marshall H. L., Nowak M. A., 2019, ApJ, 873, 29
Bothwell M. S. et al., 2013, MNRAS, 429, 3047
Brusa M. et al., 2018, A&A, 612, A29
Carilli C. L., Walter F., 2013, ARA&A, 51, 105
Chartas G., Cappi M., Hamann F., Eracleous M., Strickland S., Giustini M., Misawa T., 2016, ApJ, 824, 53
Cicone C. et al., 2014, A&A, 562, A21
Daddi E. et al., 2015, A&A, 577, A46
Duric N., Bourneuf E., Gregory P. C., 1988, AJ, 96, 81
Faucher-Giguère C.-A., Quataert E., 2012, MNRAS, 425, 605
Feruglio C., Maiolino R., Piconcelli E., Menci N., Aussel H., Lamastra A., Fiore F., 2010, A&A, 518, L155
Feruglio C. et al., 2015, A&A, 583, A99
Feruglio C. et al., 2017, A&A, 608, A30
Fischer J. et al., 2010, A&A, 518, L41
Fixsen D. J., Bennett C. L., Mather J. C., 1999, ApJ, 526, 207
Gioia I. M., Gregorini L., Klein U., 1982, A&A, 116, 164
Hartley P., Jackson N., Sluse D., Stacey H. R., Vives-Arias H., 2019, MNRAS, 485, 3009
Jackson N. et al., 2015, MNRAS, 454, 287
Kennicutt R. C., 1998, ApJ, 498, 541
Leung T. K. D., Riechers D. A., Pavesi R., 2017, ApJ, 836, 180
Longinotti A. L. et al., 2018, ApJ, 867, L11
Mizumoto M., Izumi T., Kohno K., 2019, ApJ, 871, 156
Morgan C. W. et al., 2018, ApJ, 869, 106
Oguri M., 2010, Astrophysics Source Code Library, record ascl:1010.012
Papadopoulos P. P., van der Werf P., Xilouris E., Isaak K. G., Gao Y., 2012, ApJ, 751, 10
Paraficz D. et al., 2018, A&A, 613, A34
Planck Collaboration XIII, 2016, A&A, 594, A13
Riechers D. A., 2011, ApJ, 730, 108
Rowan-Robinson M., Wang L., 2010, MNRAS, 406, 720
Runnoe J. C., Brotherton M. S., Shang Z., 2012, MNRAS, 422, 478
Rupke D. S., Veilleux S., 2005, ApJ, 631, L37
Rybak M., Vegetti S., McKean J. P., Andreani P., White S. D. M., 2015, MNRAS, 453, L26
Sirressi M. et al., 2019, MNRAS, 489, 1927
Smith R. N., Tombesi F., Veilleux S., Lohfink A. M., Luminari A., 2019, ApJ, 887, 69
Solomon P. M., Vanden Bout P. A., 2005, ARA&A, 43, 677
Stacey H. R. et al., 2018, MNRAS, 476, 5075
Sturm E. et al., 2011, ApJ, 733, L16
Tombesi F., Meléndez M., Veilleux S., Reeves J. N., González-Alfonso E., Reynolds C. S., 2015, Nature, 519, 436
van der Werf P. P. et al., 2010, A&A, 518, L42
Veilleux S. et al., 2013, ApJ, 776, 27
Veilleux S. et al., 2017, ApJ, 843, 18
Wang R. et al., 2013, ApJ, 773, 44
Zaječek M. et al., 2019, A&A, 630, A83
Zhao W., Hong X., An T., Li X., Cheng X., Wu F., 2019, Galax, 7, 86
Zubovas K., King A., 2012, ApJ, 745, L34

This paper has been typeset from a TEX/LATEX file prepared by the author.